Available online at www.sciencedirect.com

ScienceDirect

Trans. Nonferrous Met. Soc. China 32(2022) 122−133

Transactions of
Nonferrous Metals
Society of China

www.tnmsc.cn

Microstructure and mechanical properties of AZ31 alloy prepared by cyclic expansion extrusion with asymmetrical extrusion cavity

Min-jie LIANG, Jie ZHENG, Huan LIU, Bao-xing YAO

School of Materials Science and Engineering, North University of China, Taiyuan 030051, China

Received 21 November 2020; accepted 29 June 2021

Abstract: The microstructure, texture evolution and mechanical properties of AZ31 magnesium alloy were investigated during the cyclic expansion extrusion with the asymmetrical extrusion cavity (CEE-AEC) process. The results show that continuous dynamic recrystallization (CDRX) and discontinuous dynamic recrystallization (DDRX) occur during the CEE-AEC process. After 3 passes, the microstructures of the deformed samples are refined, and the average grain size of the alloys in asymmetrical cavity region is 6.9 μm. The maximum intensities of the basal textures increase with the increase in the number of passes, and the basal textures are deflected during the deformation process. The basal texture of the alloys in asymmetrical cavity region is tilted by approximately ±45° from the normal direction (ND) to the extrusion direction (ED). Grain refinement strengthening and texture deflection significantly improve the comprehensive mechanical properties of the deformed alloys. After 3 passes, tensile yield strength (TYS), ultimate tensile strength (UTS) and elongation- to-failure of the alloy in the asymmetric cavity region are 146 MPa, 230 MPa and 29.7%, respectively.

Key words: magnesium alloy; microstructure; cyclic expansion extrusion; mechanical properties; texture

1 Introduction

Magnesium alloy has attracted attention as a potential structural material due to its low density, high specific stiffness and good recyclability [1−3]. However, Mg alloy has poor room-temperature mechanical properties, due to its hexagonal close-packed (HCP) structure with limited activation sliding systems [4−6], which limits its widespread application in the aerospace and automotive industries.

Grain refinement and texture control are favored as effective methods to improve the strength and ductility of Mg and its alloys. It is well known that strength and ductility can be improved simultaneously by grain refinement according to the Hall−Petch formula [7]. Therefore, many researchers use different deformation processes to refine the grain. In recent years, severe plastic deformation techniques, such as equal channel angular pressing (ECAP) [8], accumulated extrusion bonding (AEB) [9], high pressure torsion (HPT) [10] and cyclic expansion extrusion (CEE) [11,12] have been extensively studied as effective methods for grain refinement. In addition, some researchers have changed the cavity structure of the traditional extrusion process to refine the grain and control the texture. WANG et al [13] studied the microstructure and mechanical properties of Mg alloy sheets prepared with the continuous variable channel direct extrusion (CVCDE) process and found that shear deformation can effectively promote grain refinement and improve mechanical properties. LIU et al [14] confirmed that direct extrusion and bending–shear (DEBS) deformation processes can effectively weaken the texture. XU et al [15] investigated the effect of different

---

Corresponding author: Min-jie LIANG, Tel: +86-18734159668, E-mail: 499134232@qq.com

DOI: 10.1016/S1003-6326(21)65782-5

extrusion angles on AZ31 magnesium alloy and showed that changing the extrusion angle can promote texture deflection to obtain excellent mechanical properties. The above research shows that introducing shear stress into the deformation process can effectively improve the comprehensive mechanical properties. In this regard, ECAP is a severe plastic deformation technology that introduces shear strain and has attracted many research interests. However, the dimension of the deformed billets adopting the ECAP process is usually small, which limits its wide application.

A new severe plastic deformation process, cyclic expansion extrusion with asymmetrical extrusion cavity (CEE-AEC) is proposed, which can prepare billets with length, width and height of 100, 50 and 220 mm, respectively. Because its cavity is asymmetric, the CEE-AEC process can perform upsetting, extrusion and shear deformation in a single pass, and the billets can be made by multi-pass to increase the cumulative strain. In a previous study, we revealed the effect of the CEE-AEC process on the microstructure and texture evolution of Mg−13Gd−4Y−2Zn−0.5Zr (wt.%) alloy with decreasing temperatures [16,17]. In the present work, the effect of different regions on the microstructure, texture evolution and mechanical properties of AZ31 alloy prepared by the CEE-AEC process was investigated. The mechanism of grain refinement during CEE-AEC processing is further analyzed.

2 Experimental

The material used in the present study was as-cast commercial AZ31B alloy (Mg−2.99Al−0.98Zn, in wt.%) with a width of 100 mm, a thickness of 50 mm and a length of 220 mm, and a general description for three orthogonal directions in AZ31 alloy: ED for the extrusion direction (length), TD for the transverse direction (thickness), and ND for the normal direction (width) (Fig. 1). The ingots were homogenized in an electronic furnace at 400 °C for 12 h and then air-cooled naturally. Before deformation, the ingots and dies were heated at corresponding deformation temperature for 2 h. The homogenized ingots were subjected to isothermal multi-pass extrusion deformation at 320 °C using CEE-AEC dies at extrusion speed of 1 mm/s. The graphite-based mixture was used as the lubricant during the deformation process. After each pass, the deformed billets were water quenched to maintain the microstructure. After the final extrusion pass, the samples were air cooled.

The schematic of the CEE-AEC process and the specific parameters of the cavity are shown in Fig. 1. The CEE-AEC die cavity can be divided into three different observation regions: symmetrical cavity, central cavity and asymmetrical cavity (Fig. 1). The samples for observation and the tensile samples were processed from three different regions of the deformed billets. An optical microscope (OM, Axio Observer A2m Carl Zeiss) was used to observe the microstructure of the samples, and the observation plane was the ED−TD plane. The samples for OM observation were ground on SiC paper (800$^{\#}$, 1000$^{\#}$, 2000$^{\#}$, 3000$^{\#}$ and 5000$^{\#}$), and then mechanically polished to eliminate scratches. Finally, the samples were chemically etched in the

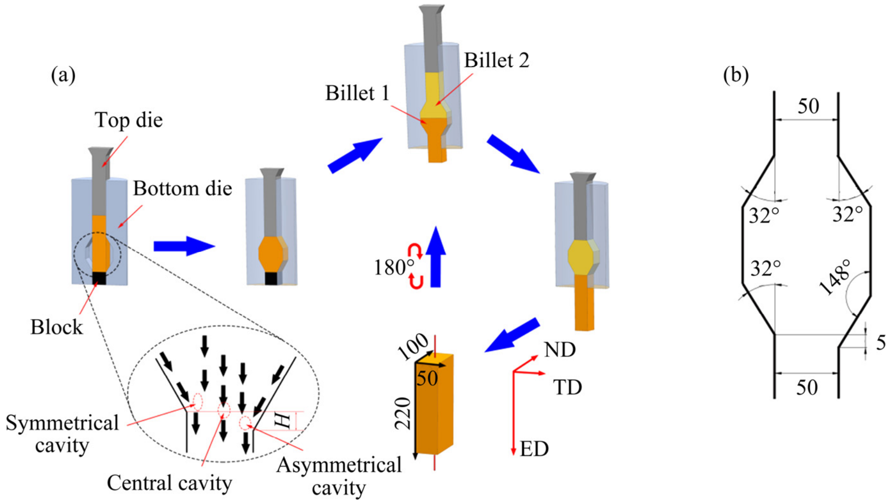

Fig. 1 Schematic diagram of CEE-AEC process (a) and specific parameters of mold cavity (b) (unit: mm)

solution of 1 g picric acid, 14 mL alcohol, 2 mL acetic acid and 2 mL distilled water. The microstructure and texture evolution of the samples were observed by electron back-scattered diffraction (EBSD, Hitachi SU5000 FE-SEM). Before EBSD observation, the samples were mechanically polished and followed by electro-polishing at a voltage of 15 V for ~120 s at −30 °C with a perchloric acid−ethanol reagent (volume ratio of 1:9). The EBSD observation was performed on the ED−TD plane of the samples, with the scanning step size of 0.6 μm, operating at 20 kV, 70° tilt angle and 15 mm working distance. The EBSD data were analyzed using orientation imaging microscopy (OIM) software 7.0. The tensile axis of the tensile specimen was parallel to the ED, and their tensile performances were tested on 3382 Instron universal material experiment machine at room-temperature with a strain rate of $0.001\ \mathrm{s}^{-1}$. To ensure the reliability of the experiments, the tensile results were calculated from the average of three replicates.

3 Finite element analysis

A finite element simulation method was performed using DEFORM-3D V 11.2 software to simulate and analyze the deformation behavior of the 1-pass CEE-AEC process. To simulate the deformation characteristics of the CEE-AEC process more accurately, the size and temperature of the working sample in the simulation software were defined as the same as in the actual experiment. In the simulation process, the top and bottom dies were defined to be rigid, and the specimen was defined to be plastic, with 200000 meshes. The friction between the dies and the specimen was set to be 0.3, the extrusion speed of the top die was set to be 1 mm/s, and the heat transfer coefficient was set to be 1.1×10^4 W/(m·K).

The effective strain distribution of AZ31B alloy during the CEE-AEC process is shown in Fig. 2(a), where it can be clearly seen that the distribution of effective strain in the edge cavity is higher than that in the central cavity. The effective strain evolutions in different deformation zones are exhibited in Fig. 2(b). Remarkably, during the 1-pass CEE-AEC process, the effective strain of the central cavity is the lowest, and the effective strain of the asymmetrical cavity is the highest, which confirms that the asymmetry of the cavity leads to the formation of a stress gradient in the TD to produce a shear force. According to the different effective strains of different deformation regions in Fig. 2, the effect of different deformation regions on microstructure, texture evolution and mechanical properties is explored by physical experiments.

4 Results and discussion

The OM microstructures of CEE-AEC samples in different regions are shown in Fig. 3. The microstructures in different regions are significantly refined compared with the homogenized billets with average grain size of 400 μm, due to the occurrence of dynamic recrystallization (DRX) during CEE-AEC processes. Table 1 lists the average grain sizes of CEE-AEC samples at 320 °C. The typical bimodal distribution of microstructures and the original coarse deformed grains are surrounded by fine grains, as shown in Figs. 3(a, d, g). The serrated grain boundaries (marked as white dashed

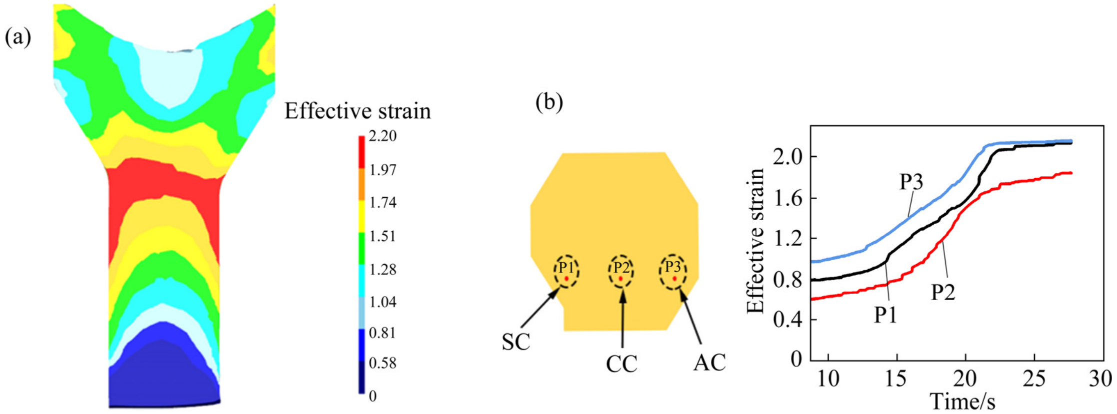

Fig. 2 Finite element simulation of 1-pass CEE-AEC process: (a) Effective strain distribution; (b) Effective strain evolutions in different deformation zones (SC−Symmetrical cavity, CC−Central cavity, AC−Asymmetrical cavity)

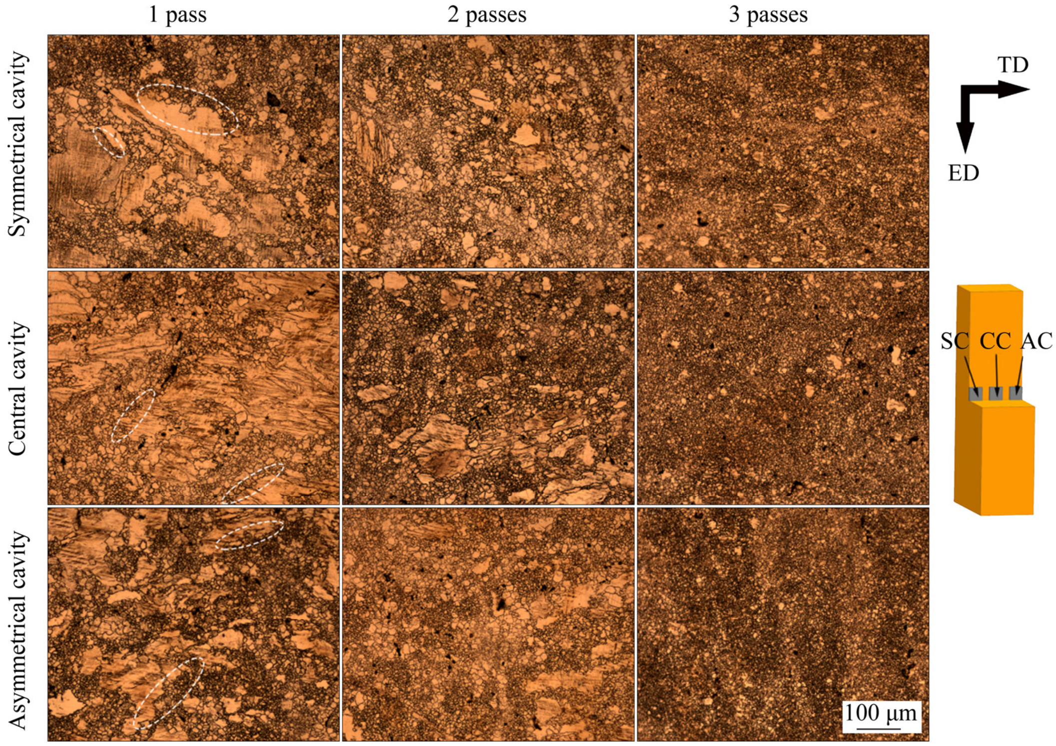

Fig. 3 OM microstructures of CEE-AEC samples at 320 °C

Table 1 Average grain sizes of CEE-AEC samples

Sample	Average grain size/μm		
	1 pass	2 passes	3 passes
SC	26.2±2.1	12.7±1.7	7.1±0.8
CC	30.1±2.5	15.9±1.9	7.8±1.2
AC	23.1±2.3	10.4±1.5	6.9±0.4

circles) can be observed along the coarse grains and many fine grains nucleate at the grain boundaries of coarse grains, which indicates that DRX has occurred during 1-pass CEE-AEC process [18]. The strain imbalance in the high dislocation density region during the deformation process leads to the local migration and expansion of the grain boundaries, which leads to the formation of serrated grain boundaries. After 1 pass, the average grain sizes of the microstructures of the symmetrical cavity (SC), the central cavity (CC) and the asymmetrical cavity (AC) are 26.2, 30.1 and 23.1 μm, respectively. The above results are consistent with the equivalent strain distribution results in Fig. 2. As seen in Figs. 3(b, e, h), the coarse grains are refined, the microstructures become more homogeneous, and the average grain size of the alloy in the asymmetrical cavity region is 10.4 μm. As the number of CEE-AEC passes increases, the coarse grains disappear and microstructures are almost composed of homogeneous equiaxed grains. The average grain sizes of the symmetrical cavity region, central cavity region and asymmetrical cavity region are refined from 12.7, 15.9 and 10.4 μm (2 passes) to 7.1, 7.8 and 6.9 μm (3 passes), respectively.

The EBSD maps and (0001) pole figures of CEE-AEC samples are shown in Fig. 4 and Fig. 5, respectively. The low angle grain boundaries (LAGBs) with misorientation angles between 2° and 15° (marked with the white lines), and the high angle grain boundaries (HAGBs) with misorientation angles larger than 15° (shown by the black lines), are demonstrated in Fig. 4. The volume fractions of DRXed grains in different regions obtained from EBSD results are shown in Table 2. Mg and its alloys, with low stacking fault energy, are prone to DRX during thermal deformation [19]. In the early stage of CEE-AEC deformation, the volume fractions of DRXed grains are low, because DRX is related to cumulative strain [20]. As the CEE-AEC passes increase, the cumulative strain increases, resulting in an increase in the volume fraction of DRXed grains. The volume fraction of DRXed grains of the symmetrical cavity region increases from 38.6% (1 pass) to 85.4% (3 passes),

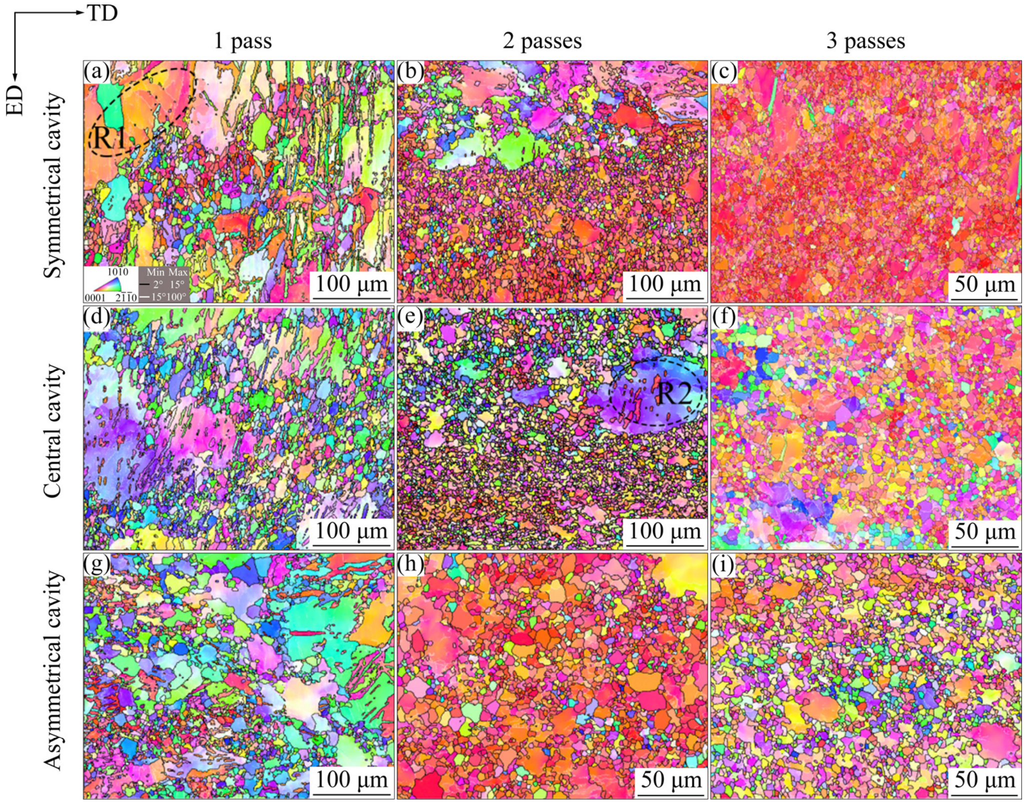

Fig. 4 EBSD IPF maps of CEE-AEC samples at 320 °C

and the corresponding region is almost completely DRXed. In addition, according to the analysis of the finite element simulation results, the effective strain of the asymmetrical cavity during CEE-AEC deformation is the largest, while that of the central cavity is the smallest. This corresponds to the data in Table 2. After 3 passes, the volume fractions of DRXed grains of the central cavity and the asymmetrical cavity are 80.3% and 91.6%, respectively.

Figure 5 depicts the (0001) pole figures of the CEE-AEC samples on the ED−TD plane at 320 °C. The maximum intensity of the basal texture of the central cavity region is 11.683, which is the largest of the three regions after 1 pass. And the maximum intensities of the asymmetrical cavity region and the symmetrical cavity region are 9.944 and 7.051, respectively. As the number of passes increases, the maximum intensities of the basal texture of the symmetrical cavity region, the central cavity region and the asymmetrical cavity region are 15.457, 13.502 and 19.758 (2 passes), respectively. Although the maximum intensities of the basal texture in the three regions are different, the texture evolution law is similar. After 1 pass, the basal texture distribution is scattered, which is due to the random orientation of the fine DRX grains caused by cumulative strain [19]. The grains rotate in the same trend during the CEE-AEC deformation, due to the existence of shear strain caused by the asymmetry of the cavity in the CEE-AEC dies. As the number of deformation passes increases, the grain orientation gradually tends to be consistent. Furthermore, although the shear deformation occurs in different regions during the deformation process, the shear strains in different regions are different. In other words, the deflection tendency of the grains in different regions is the same, but the deflection angles are different. After 3 passes, the maximum intensity of the basal texture of the central cavity region is 18.726, which presents the lowest basal intensity of the three regions, and it tilts by approximately ±35° from ND to ED (Fig. 5(f)). Figure 5(g) reveals that the basal texture of the asymmetrical cavity region is inclined about ±45° from ND to ED, and the maximum intensity is 22.842, which is the highest of the three regions. The maximum intensity of the basal texture of the

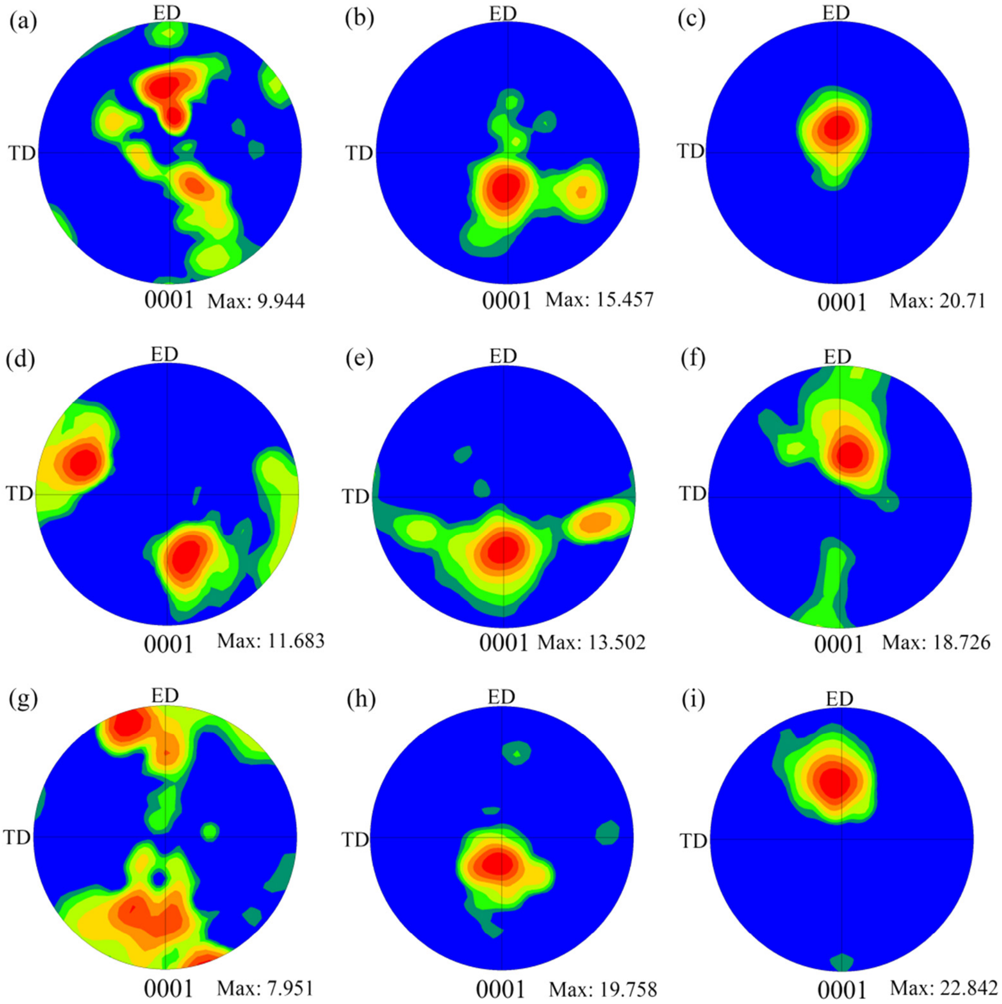

Fig. 5 (0001) pole figures of CEE-AEC samples at 320 °C: (a−c) Symmetrical cavity; (d−f) Central cavity; (g−i) Asymmetrical cavity; (a, d, g) 1 pass; (b, e, h) 2 passes; (c, f, i) 3 passes

Table 2 Volume fraction of DRXed grains

Sample	DRX fraction/%		
	1 pass	2 passes	3 passes
SC	38.6	60.3	85.4
CC	33.5	56.4	80.3
AC	43.7	67.6	91.6

symmetrical cavity region is 20.71, and its inclination angle is approximately ±20° from ND to ED (Fig. 5(c)). At present, controlling the texture is mainly to weaken the intensity of the basal texture and change the texture deflection angle [21]. Some studies have shown that the addition of rare earth elements can effectively weaken the basal texture and improve the mechanical properties [22]. For AZ31 alloy, the ductility is usually improved by changing the deflection angle of the basal texture. Many studies have obtained high-performance alloys by texture weakening with deflection. XU et al [23] prepared the high-performance AZ31 alloy sheet through the slope extrusion process, which has an unusual texture with a deflection double-peak feature. TU et al [24] prepared AZ31 alloy with Zn-texture using equal channel angular rolling and continuous bending, which improved the mechanical properties by weakening and deflecting the basal texture. The weakening of the texture increases the ductility, but the strength of the material deteriorates [25]. There are few studies related to improving the mechanical properties by increasing the deflection angle of the basal texture while also enhancing its maximum intensity.

Figure 6 shows the $(0001)\langle 11\bar{2}0\rangle$ Schmid factor distribution maps of the CEE-AEC samples. Table 3 lists the average values of $(0001)\langle 11\bar{2}0\rangle$ Schmid factors of the CEE-AEC samples. After 1 pass, the Schmid factor distribution map of the symmetrical cavity region exhibits a peak of over 0.4, with an average value of 0.36 (Fig. 6(a)). The average values of the Schmid factors of the central cavity region and the asymmetrical cavity region are 0.35 and 0.36, respectively. As the number of passes increases, the Schmid factors of different regions change. After 3 passes, the peak value of the Schmid factor of the symmetrical cavity region is between 0.3 and 0.4, and the average value is 0.3 (Fig. 6(c)). For the central cavity region, the peak value of the Schmid factor is between 0.4 and 0.5, and for the asymmetric cavity region the peak value reaches 0.5. The average values of the samples for the asymmetrical cavity region and the central cavity region are increased to 0.43 and 0.39, respectively. Due to the similar basal texture intensities of the 3 passes CEE-AEC samples, the difference in Schmid factors may be mainly due to the different inclination angles of the basal texture from ND to ED [26]. At room temperature, basal slip is dominant, so the Schmid factors of the (0001) basal determines whether the basal slip is activated in the AZ31 alloy.

The grain refinement mechanism of the alloys during the CEE-AEC processing was further analyzed. Figure 7(a) reveals the DRX behavior of the deformed grains during 1 pass in the Region R1 (highlighted by a dashed circle in Fig. 4(a)), and the point-to-point misorientation angles and the point-to-origin misorientation angles of the Arrows *A*−*B* and *C*−*D* shown in Figs. 7(b) and 7(c), respectively. During the deformation process, the point-to-origin misorientation angle changes are caused by the rotation of the crystal lattices. The point-to-point misorientation angle of Arrow *A*−*B* gradually increases to 20.7°, which indicates that the orientation changes continuously in the deformed grain (Fig. 7(b)). The dislocation density gradually increases and migrates as the cumulative strain increases during deformation. Many LAGBs can improve their misorientation angle by trapping the moving dislocations and transform to HAGBs to form new fine DRXed grains (marked by white arrows), which is a typical continuous dynamic

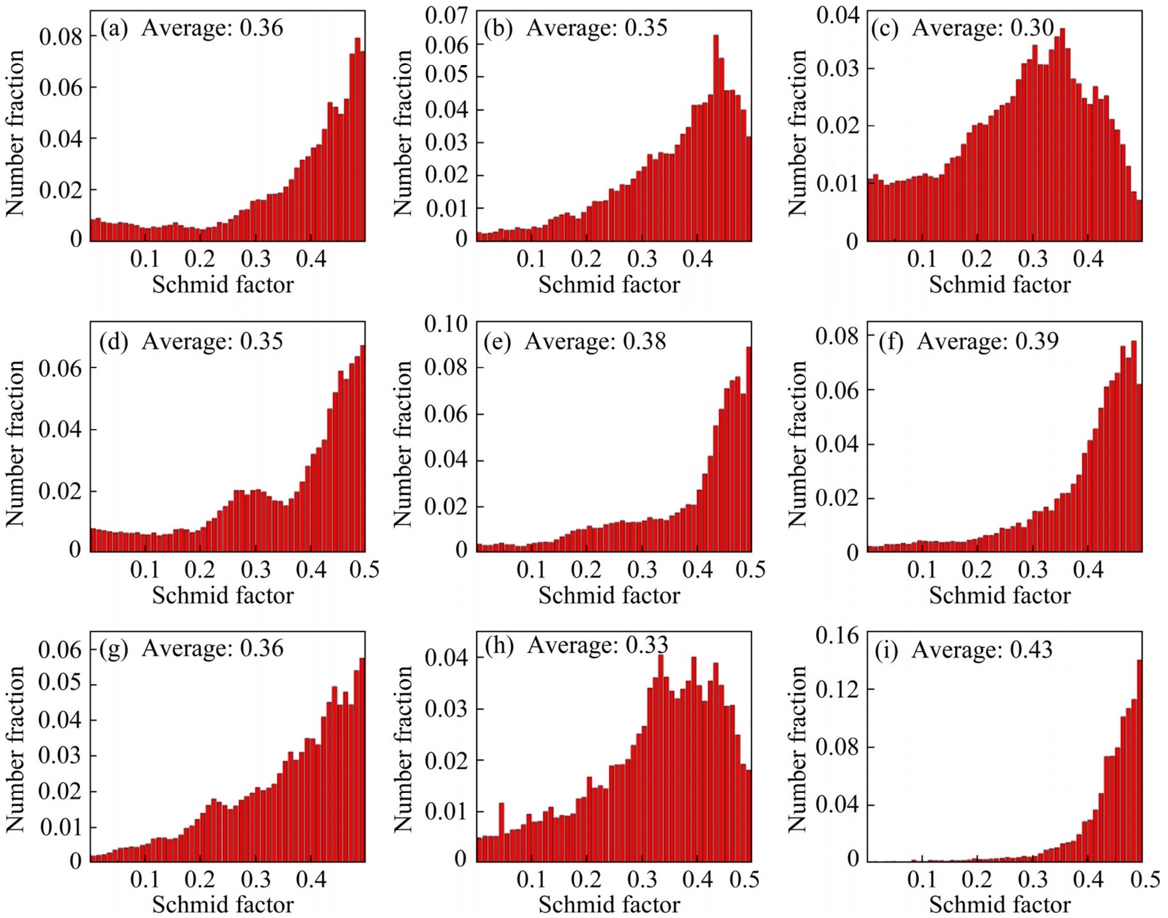

Fig. 6 $(0001)\langle 11\bar{2}0\rangle$ Schmid factor distribution of CEE-AEC samples at 320 °C: (a−c) Symmetrical cavity; (d−f) Central cavity; (g−i) Asymmetrical cavity; (a, d, g) 1 pass; (b, e, h) 2 passes; (c, f, i) 3 passes

Table 3 Average values of $(0001)\langle 11\bar{2}0\rangle$ Schmid factor of CEE-AEC samples

Samples	1 pass	2 passes	3 passes
SC	0.36	0.35	0.30
CC	0.35	0.38	0.39
AC	0.36	0.33	0.43

recrystallization (CDRX) mechanism [27]. The point-to-origin misorientation angle of Arrow *E*−*F* in Region R2 (highlighted by a dashed circle in Fig. 4(e)) indicates that the CDRX mechanism also occurs in the remaining coarse grains during 2 passes (Fig. 7(d)). Moreover, some sub-grains (marked by black arrows) at the serrated grain boundaries are separated from coarse grains through LAGBs to form DRXed grains, which is a typical discontinuous dynamic recrystallization (DDRX) mechanism [28]. This is due to the high-density dislocations sliding near the grain boundaries of the coarse grains, resulting in a large strain gradient. The dislocation sources of the grain boundaries release the non-basal dislocation slip into the inside of the grain to adapt to the deformation. Subsequently, these dislocations interact with the basal slip dislocations to form sub-grain boundaries, cutting off the protrusions on the coarse grain boundaries. As the deformation intensifies, these sub-grains trap mobile dislocations and gradually high-angle grain boundaries are formed. The point-to-point misorientation angles of Arrows *C*−*D* and *E*−*F* contain 86°, consistent with the definition of twins [29], indicating that twinning occurs during the deformation process.

The true stress−strain curves of as-cast and 3 passes samples are illustrated in Fig. 8. The corresponding mechanical properties including tensile yield strength (TYS), ultimate tensile strength (UTS) and elongation-to-failure (EF) are listed in Table 4. The TYS, UTS and EF of as-cast samples are 64 MPa, 147 MPa and 15.7%, respectively. After 3 passes, the UTS and EF of the asymmetrical cavity are 230 MPa and 29.7%, respectively. Compared with the as-cast sample, the mechanical properties of the samples in different regions combine excellent strength and ductility. However, their comprehensive mechanical properties are still slightly different, mainly affected by grain size and texture. In this study, the average grain sizes of the symmetrical cavity, central cavity and asymmetrical cavity are 7.1, 7.8 and 6.9 μm, respectively. According to Hall−Petch relationship, the enhancement of strength is mainly due to grain refinement strengthening [30]. Grain refinement enhances the resistance of dislocation motion during plastic deformation [31]. But the TYS of the

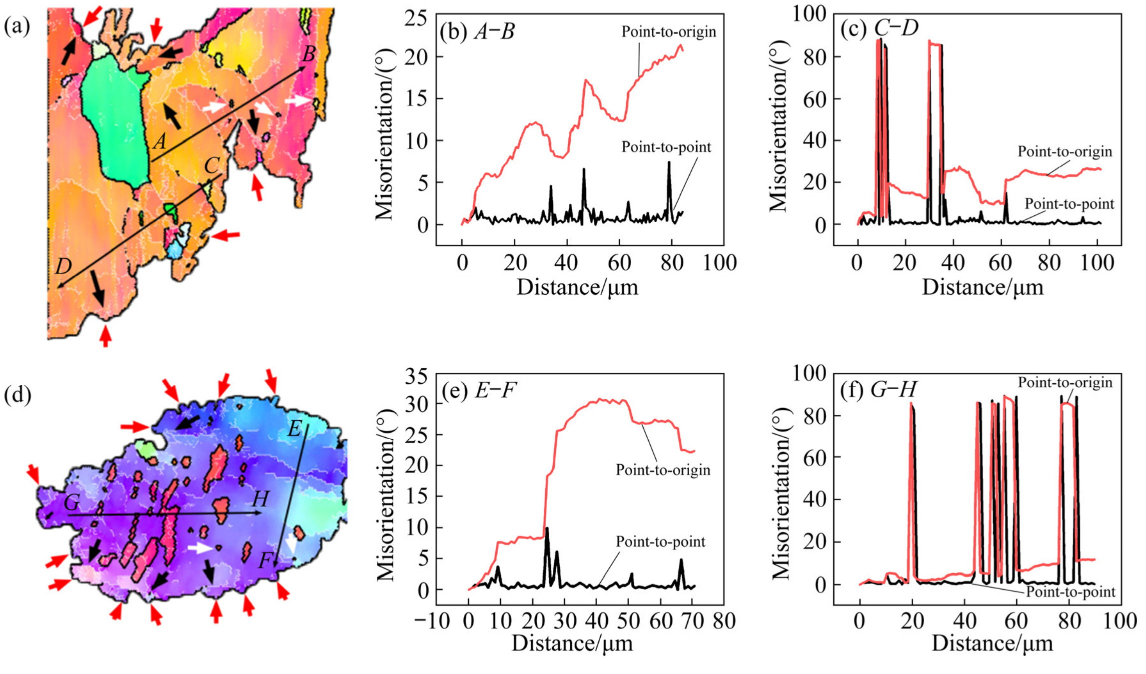

Fig. 7 EBSD IPF map of Region R1 in Fig. 4 (a) and line profiles of misorientation angle along *A*−*B* (b) and *C*−*D* (c), respectively; EBSD IPF map of Region R2 in Fig. 4 (d) and line profiles of misorientation angle along *E*−*F* (e) and *G*−*H* (f), respectively

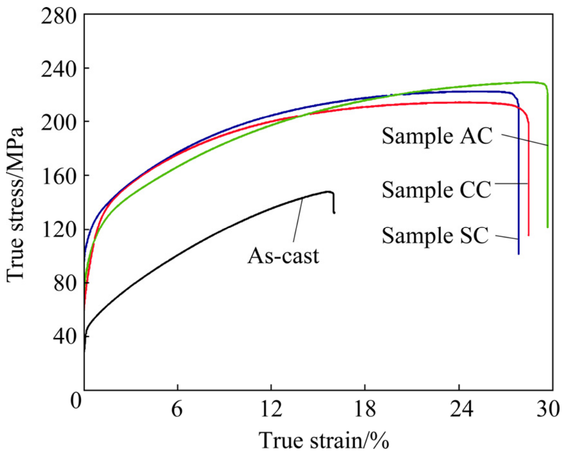

Fig. 8 True stress−strain curves of samples

Table 4 Mechanical properties of samples

Sample	TYS/MPa	UTS/MPa	EF/%
As-cast	64±1.5	147±2.3	15.7±0.7
SC	155±1.4	221±1.7	27.8±0.9
CC	154±2.1	214±2.6	28.4±1.1
AC	146±1.9	230±1.2	29.7±1.3

alloy in the asymmetrical cavity region is 146 MPa, which is the lowest of the three regions. Therefore, the texture evolution has an opposite effect on the TYS of the deformed sample. Table 3 reveals that in the three regions after 3 passes, the average value of the Schmid factor of the asymmetrical cavity region reaches 0.43, which is the highest. It is well known that the critical resolved shear stress (CRSS) of basal slip systems is related to Schmid factor [32]. The larger the Schmid factor is, the smaller the CRSS of the basal slip is, and the basal slip is more easily activated during stretching, which is beneficial to increasing the ductility but reducing the TYS. In general, the average grain size of the asymmetric cavity region of the alloy is the finest, but the basal slip is easy to activate due to the high Smith factor, and it is difficult to hinder the dislocation slip, so the TYS of the alloy in the asymmetric cavity region is the lowest but the ductility is the most outstanding. Furthermore, after 3 passes, TYS and EF of the alloy in symmetrical cavity region are 155 MPa and 27.8%, respectively. The main reason is that the lowest average value of the Schmid factor makes it relatively difficult to activate the basal slip, and the relatively medium average grain size and texture strength result in the symmetrical area having the highest YS.

Figure 9 shows the fracture morphologies of as-cast and 3-passes samples after being stretched to failure along ED at room temperature. The fracture morphology consists of cleavage planes and a few dimples, as presented in Fig. 9(a). The ductility of deformed samples is gradually

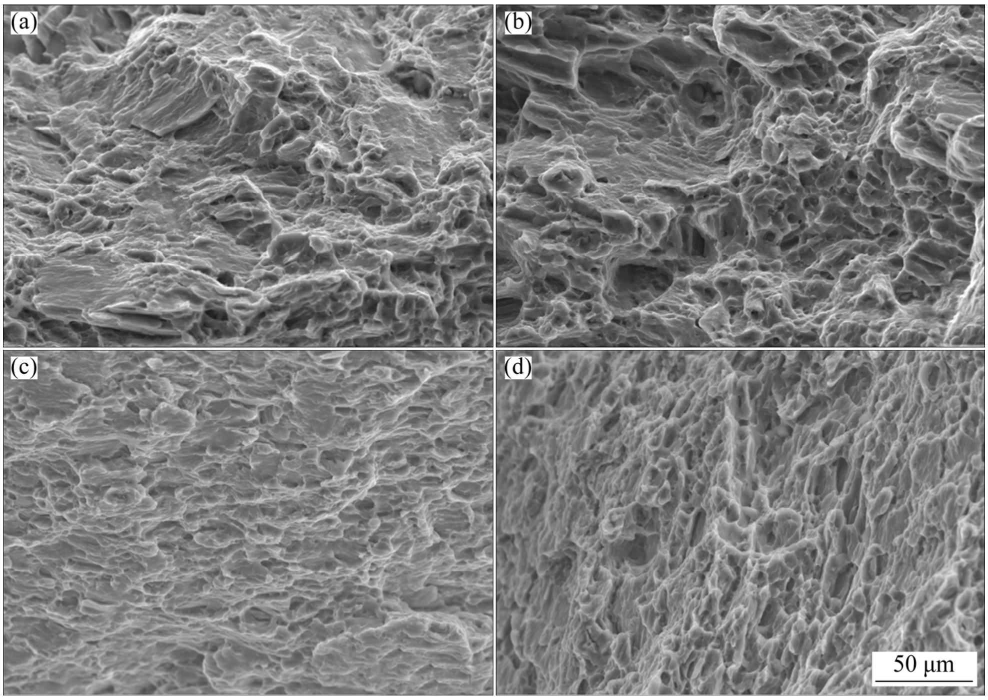

Fig. 9 SEM images of fracture morphologies of as-cast and 3 passes samples: (a) As-cast; (b) Sample SC; (c) Sample CC; (d) Sample AC

improved with an increase in the number of passes. After 3 passes, there are many dimples in the fracture morphologies of the deformed samples, which are typical ductile fractures. In summary, the grain refinement strengthening and inclined texture of the deformed samples effectively improve the comprehensive mechanical properties of AZ31 alloy at room temperature.

5 Conclusions

(1) Compared with other regions, the effective strain of alloy in the asymmetrical cavity region during the deformation is the largest, and the average grain size of 6.9 μm was obtained after 3 passes. The average grain sizes in the symmetrical cavity and the central cavity regions are 7.1 μm and 7.8 μm, respectively.

(2) Grain refinement of deformed alloy is mainly determined by DRX, CDRX and DDRX simultaneously occurring during CEE-AEC deformation. After 3 passes, the volume fraction of DRXed grains in the asymmetrical cavity reaches 91.6%.

(3) The basal texture deflects from ND to ED during the deformation process, and the maximum intensity gradually increases. The deflection angle of the asymmetrical cavity is approximately ±45°, which is the largest of the three regions. The deflection angles of the basal texture of the symmetrical cavity and the central cavity are ±35° and ±20°, respectively.

(4) After 3 passes, the UTS, TYS and EF of the asymmetrical cavity are 146 MPa, 230 MPa and 29.7%, respectively. Compared with as-cast samples, the mechanical properties of deformed samples are significantly improved, which are mainly affected by grain refinement and deflection texture.

Acknowledgments

The authors are grateful for the financial supports from International Science and Technology Cooperation Program of Shanxi Province, China (No. 201603D421024); Shanxi Scholarship Council of China (No. 2017-095).

References

[1] PENG Yong-gang, DU Zhi-wei, LIU Wei, LI Yong-jun, LI Ting, HAN Xiao-lei, MA Ming-long, PANG Zheng, YUAN Jia-wei, SHI Guo-liang. Evolution of precipitates in Mg−7Gd−3Y−1Nd−1Zn−0.5Zr alloy with fine plate-like 14H-LPSO structures aged at 240 °C [J]. Transactions of Nonferrous Metals Society of China, 2020, 30: 1500−1510.

[2] ALIYARI Sh, FATEMI S M, MIRESMAEILI S M. Effects of solution treatment on high temperature deformation behavior of extruded Mg−0.35Y−2.17Nd−0.36Zr biomedical alloy [J]. Transactions of Nonferrous Metals Society of China, 2019, 29: 1842−1853.

[3] XIA Da-biao, ZHANG Jun-lei, CHEN Xiang, HUANG Guang-sheng, JIANG Bin, TANG Ai-tao, GAVRAS S, HUANG Y, HORT N, PAN F. Effect of biaxial compressive stress state on the microstructure evolution and deformation compatibility of rolled sheet Mg alloy AZ31 at room temperature [J]. Materials Science and Engineering A, 2020, 789: 139599.

[4] JIA Qing-gong, ZHANG Wen-xin, SUN Yi, XU Chun-xiang, ZHANG Jin-shan, KUAN Jun. Microstructure and mechanical properties of as-cast and extruded biomedical Mg−Zn−Y−Zr−Ca alloy at different temperatures [J]. Transactions of Nonferrous Metals Society of China, 2019, 29: 515−525.

[5] MA Ru, LU Yue, WANG Ling, WAG Yi-nong. Influence of rolling route on microstructure and mechanical properties of AZ31 magnesium alloy during asymmetric reduction rolling [J]. Transactions of Nonferrous Metals Society of China, 2018, 28: 902−911.

[6] WU Yi-ping, XIONG Han-qing, JIA Yu-zhen, XIE Shao-hui, LI Guo-feng. Microstructure, texture and mechanical properties of Mg−8Gd−4Y−1Nd−0.5Zr alloy prepared by pre-deformation annealing, hot compression and ageing [J]. Transactions of Nonferrous Metals Society of China, 2019, 29: 976−983.

[7] WANG Yan-peng, Li Feng, SHI Wen-yong, LI Xue-wen, FANG Wen-bin. Microstructure, bending behavior and texture evolution of AZ31B magnesium alloy bending products processed by staggered extrusion (SE) [J]. Materials Characterization, 2019, 155: 109842.

[8] YAN Kai, SUN Jia-peng, LIU Huan, CHENG Hong-hui, BAI Jing, HUANG Xin. Exceptional mechanical properties of an Mg97Y2Zn1 alloy wire strengthened by dispersive LPSO particle clusters [J]. Materials Letters, 2019, 242: 87−90.

[9] HAN Ting-zhuang, HUANG Guang-sheng, DENG Qian-yuan, WANG Guan-gang, JIANG Bin, TANG Ai-tao, ZHU Yun-tian, PAN Fu-sheng. Grain refining and mechanical properties of AZ31 alloy processed by accumulated extrusion bonding [J]. Journal of Alloys and Compounds, 2018, 745: 599−608.

[10] WANG Jin-hui, LI Yan-sheng, XU Rui. The thermal stability and activation energy of the nanocrystalline Mg−Zn−Y alloy obtained by high pressure torsion [J]. Materials Letters, 2020, 268: 127607.

[11] PEYGHAN R A, JAFARZADEH H. Study of fine-grained pure copper fabrication by cyclic contraction/expansion extrusion (CCEE) using experimental and finite element simulation methods [J]. Transactions of the Indian Institute of Metals, 2019, 72: 757−765.

[12] HATAMI SADR M, JAFARZADEH H. Characterization of

AZ91 magnesium alloy processed by cyclic contraction/expansion extrusion using the experimental and micromechanical cellular automaton finite element approach [J]. Proceedings of the Institution of Mechanical Engineers Part L: Journal of Materials: Design and Applications, 2020, 234: 1417−1430.

[13] WANG Ye, LI Feng, Li Xue-wen, FANG Wen-bin. Unusual texture formation and mechanical property in AZ31 magnesium alloy sheets processed by CVCDE [J]. Journal of Materials Processing Technology, 2020, 275: 116360.

[14] LIU Xiao-ye, LU Li-wei, SHENG Kun, ZHOU Tao. Microstructure and texture evolution during the direct extrusion and bending−shear deformation of AZ31 magnesium alloy [J]. Acta Metallurgica Sinica (English Letters), 2019, 32: 710−718.

[15] XU Jun, YANG Tian-hao, JIANG Bin, SONG Jiang-feng, HE Jun-jie, WANG Qing-hang, CHAI Yang-fu, HUANG Guang-sheng, PAN Fu-sheng. Improved mechanical properties of Mg−3Al−1Zn alloy sheets by optimizing the extrusion die angles: Microstructural and texture evolution [J]. Journal of Alloys and Compounds, 2018, 762: 719−729.

[16] YAN Zhao-ming, ZHANG Zhi-min, LI Xu-bin, XU Jian, WANG Qiang, ZHANG Guan-shi, ZHENG Jie, FAN Hong-zhi, XU Kai-hua, ZHU Jia-xuan, XUE Yong. A novel severe plastic deformation method and its effect on microstructure, texture and mechanical properties of Mg−Gd−Y−Zn−Zr alloy [J]. Journal of Alloys and Compounds, 2020, 822: 153698.

[17] ZHENG Jie, YAN Zhao-ming, YU Jian-min, ZHANG Zhi-min, FAN Hong-zhi, Xu Kai-hua, XUE Yong. Microstructure and mechanical properties of Mg−Gd−Y−Zn−Zr alloy by cyclic expansion-extrusion with an asymmetrical extrusion cavity (CEE-AEC) [J]. Materials Research Express, 2019, 6: 1065c8.

[18] ZHANG Hang, WANG Hui-yuan, WANG Jin-guo, RONG Jian, ZHA Min, WANG Cheng, MA Pin-kui, JIANG Qi-chuan. The synergy effect of fine and coarse grains on enhanced ductility of bimodal-structured Mg alloys [J]. Journal of Alloys and Compounds, 2019, 780: 312−317.

[19] JIANG M G, XU C, YAN H, FAN G H, NAKATA T, LAO C S, CHEN R S, KAMADO S, HAN E H, LU B H. Unveiling the formation of basal texture variations based on twinning and dynamic recrystallization in AZ31 magnesium alloy during extrusion [J]. Acta Materialia, 2018, 157: 53−71.

[20] WANG Feng-hua, SU Peng, QIN Lin-xin, DONG Shuai, LI Yun-liang, DONG Jie. Microstructure and mechanical properties of Mg–3Al–Zn magnesium alloy sheet by hot shear spinning [J]. Acta Metallurgica Sinica (English Letters), 2020, 33: 1226−1234.

[21] WANG Qing-hang, JIANG Bin, TANG Ai-tao, FU Jie, JIANG Zhong-tao, SHENG Hao-ran, ZHANG Ding-fei, HUANG Guang-sheng, PAN Fu-sheng. Unveiling annealing texture formation and static recrystallization kinetics of hot-rolled Mg−Al−Zn−Mn−Ca alloy [J]. Journal of Materials Science & Technology, 2020, 43: 104−118.

[22] HUANG Wei-ying, YANG Xu-yue, YANG Yi, MUKAI T, SAKAI T. Effect of yttrium addition on the hot deformation behaviors and microstructure development of magnesium alloy [J]. Journal of Alloys and Compounds, 2019, 786: 118−125.

[23] XU Jun, JIANG Bin, SONG Jiang-feng, HE Jun-jie, GAO Peng, LIU Wen-jun, YANG Tian-hao, HUANG Guang-sheng, PAN Fu-sheng. Unusual texture formation in Mg–3Al–1Zn alloy sheets processed by slope extrusion [J]. Materials Science and Engineering A, 2018, 732: 1−5.

[24] TU Jian, ZHOU Tao, LIU Lei, SHI Lai-xin, HU Li, SONG Deng-hui, SONG Bo, YANG Ming-bo, CHEN Qiang, PAN Fu-sheng. Effect of rolling speeds on texture modification and mechanical properties of the AZ31 sheet by a combination of equal channel angular rolling and continuous bending at high temperature [J]. Journal of Alloys and Compounds, 2018, 768: 598−607.

[25] XIAO Bi-quan, SONG Jiang-feng, TANG Ai-tao, JIANG Bin, SUN Wen-yan, LIU Qiang, ZHAO Hua, PAN Fu-sheng. Effect of pass reduction on distribution of shear bands and mechanical properties of AZ31B alloy sheets prepared by on-line heating rolling [J]. Journal of Materials Processing Technology, 2020, 280: 116611.

[26] WANG Bao-jie, XU Dao-kui, SHENG Li-yuan, HAN En-hou, SUN Jie. Deformation and fracture mechanisms of an annealing-tailored “bimodal” grain-structured Mg alloy [J]. Journal of Materials Science & Technology, 2019, 35: 2423−2429.

[27] LIN Y C, ZHU X H, DONG W Y, YANG H, XIAO Y W, KOTKUNDE N. Effects of deformation parameters and stress triaxiality on the fracture behaviors and microstructural evolution of an Al−Zn−Mg−Cu alloy [J]. Journal of Alloys and Compounds, 2020, 832: 154988.

[28] ZHA Min, ZHANG Hong-min, YU Zhi-yuan, ZHANG Xuan-he, MENG Xiang-tao, WANG Hui-yuan, JIANG Qi-chuan. Bimodal microstructure—A feasible strategy for high-strength and ductile metallic materials [J]. Journal of Materials Science & Technology, 2018, 34: 257−264.

[29] HOU De-wen, ZHU Yu-zhi, LI Qi-zhen, LIU Tian-mo, WEN Hai-ming. Effect of $\{10\overline{1}2\}$ twinning on the deformation behavior of AZ31 magnesium alloy [J]. Materials Science and Engineering A, 2019, 746: 314−321.

[30] ZHAO Guang-wei, FAN Jian-feng, ZHANG Hua, ZHANG Qiang, YANG Jie, DONG Hong-biao, XU Bing-she. Exceptional mechanical properties of ultra-fine grain AZ31 alloy by the combined processing of ECAP, rolling and EPT [J]. Materials Science and Engineering A, 2018, 731: 54−60.

[31] WEI Jian-sheng, JIANG Shu-nong, CHEN Zhi-yong, LIU Chu-ming. Increasing strength and ductility of a Mg−9Al alloy by dynamic precipitation assisted grain refinement during multi-directional forging [J]. Materials Science and Engineering A, 2020, 780: 139192.

[32] WANG Qing-hang, SONG Jiang-feng, JIANG Bin, TANG Ai-tao, CHAI Yan-fu, YANG Tian-hao, HUANG Guang-sheng, PAN Fu-sheng. An investigation on microstructure, texture and formability of AZ31 sheet processed by asymmetric porthole die extrusion [J]. Materials Science and Engineering A, 2018, 720: 85−97.

非对称挤压腔循环膨胀挤出法制备 AZ31 合金的显微组织和力学性能

梁敏洁，郑 杰，刘 欢，姚宝星

中北大学 材料科学与工程学院，太原 030051

摘 要：研究 AZ31 合金在非对称挤压腔循环膨胀挤出(CEE-AEC)过程中的显微组织、织构演化和力学性能。结果表明，在 CEE-AEC 过程中发生连续动态再结晶(CDRX)和不连续动态再结晶(DDRX)。经过 3 道次变形后，变形试样的显微组织得到细化，非对称型腔区域合金的平均晶粒尺寸为 6.9 μm。随着道次的增加，基体织构的最大强度增大，并且变形过程中基体织构发生偏转。非对称型腔区域合金的基底织构从法向(ND)到挤压方向(ED)倾斜约±45°。晶粒细化强化和织构偏转显著提高变形合金的综合力学性能。3 道次后，非对称型腔区域合金的拉伸屈服强度、极限抗拉强度和断裂伸长率分别为 146 MPa、230 MPa 和 29.7%。

关键词：镁合金；显微组织；循环膨胀挤出；力学性能；织构

(Edited by Bing YANG)